Chemical tracer diffusion of Sr and Co in polycrystalline Ca-deficient $CaMnO_{3-\delta}$ with $CaMn_2O_4$ precipitates

Temesgen D. Desissa[§], Nikola Kanas[*], Sathya P. Singh[*], Kjell Wiik[*], Mari-Ann Einarsrud[*], Truls Norby[§,1]

[§]*Department of Chemistry, Centre for Materials Science and Nanotechnology, University of Oslo, FERMiO, Gaustadalléen 21, NO-0349 Oslo, Norway*

[*]*Department of Materials Science and Engineering, NTNU Norwegian University of Science and Technology, NO-7491 Trondheim, Norway*

Abstract

Diffusivity on the A- and B-site of polycrystalline perovskite $CaMnO_{3-\delta}$ with Ca deficiency and spinel $CaMn_2O_4$ (marokite) as a secondary phase was studied using chemical tracers and secondary ion mass spectrometry (SIMS) complemented by electron probe microanalysis (EPMA). Thin films containing Sr and Co chemical tracers were deposited on the polished surface of the polycrystalline composite sample followed by annealing at $800 - 1200$ °C for 96 h. Diffusion profiles for each tracer were determined with SIMS, followed by calculation of diffusion coefficients by fitting to appropriate models. The Sr tracer showed mainly lattice diffusion, with an activation energy of 210 ± 30 kJ/mol, whereas the Co tracer showed a combination of lattice and enhanced grain-boundary diffusion, with activation energies of 270 ± 30 kJ/mol and 380 ± 40 kJ/mol, respectively. The diffusivities may be used to predict interdiffusion and lifetime of junctions between n-type $CaMnO_{3-\delta}$ or $CaMnO_{3-\delta}/CaMn_2O_4$ composites and metallization interlayers or p-type leg materials in oxide thermoelectrics. In particular, the relatively high effective diffusivity of Co in polycrystalline $CaMnO_{3-\delta}$ may play a role in the reported fast formation of the secondary phase ($Ca_3Co_{2-y}Mn_yO_6$) between p-type $Ca_3Co_{3.92}O_{9-\delta}$ and n-type $CaMnO_{3-\delta}$ in a direct *p-n* thermoelectric junction.

Introduction

---

[1] Corresponding author, E-mail: truls.norby@kjemi.uio.no

Thermoelectric generators (TEGs) utilize the different thermoelectric (Seebeck) coefficients of p- and n-type material couples to generate electricity from e.g. renewable or waste heat[1]. The legs of the traditional TEGs are connected thermally in parallel and electrically in series, with metallic interconnects to ensure ohmicity of the contacts[2]. The metallic interconnects add cost and have degradation issues from oxidation, inter-diffusion, and thermal expansion coefficient (TEC) mismatch at the metal/semiconductor interface. Alternatives are hence explored along various approaches.

Since a few years, there has been an interest in developing wide-area direct p-n junction-based thermoelectric modules[3]. Similarly, we propose direct p-n junctions between oxide thermoelectric materials to develop high-temperature TEGs without the use of metallic interconnects. Cobalt-based oxide thermoelectric materials exhibit the best p-type properties comprising, for example, the misfit layered oxide $Ca_3Co_{3.92}O_{9-\delta}$ (CCO)[4, 5]. Among the few n-type oxide-based thermoelectric materials we find the perovskite-structured $CaMnO_{3-\delta}$ (CM)[6]. We are presently exploring enhanced thermoelectric properties of nominally Ca-deficient CM, where the perovskite coexists with precipitates of the spinel (marokite) phase, $CaMn_2O_4$, to be published elsewhere.

It has recently been shown that when a p-n heterojunction is formed directly between p-type CCO and n-type nominally Ca-deficient CM, a secondary phase $Ca_3Co_{2-y}Mn_yO_6$ (CCMO) is formed[7], requiring inter-diffusion of Ca, Mn, and Co.

In order to contribute to the evaluation of the lifetime of direct p-n junctions between CCO and CM in thermoelectrics as well as other applications such as for electro-catalysis in Li-O$_2$ batteries[8, 9], we herein report on a study of A- and B-site diffusivities in nominally Ca-deficient $CaMnO_{3-\delta}$. The oxide selected in the present work was a composite of 90 vol% perovskite $CaMnO_{3-\delta}$ and 10 vol% marokite ($CaMn_2O_4$) corresponding to the overall stoichiometry $Ca_{0.934}MnO_{3-\delta}$, hereafter abbreviated as CMO. Sr and Co were selected as chemical tracers for Ca and Mn, respectively, on the A- and B-sites of the perovskite. The ionic radii of these chemical tracers are $r(Sr^{2+}) = 0.126$ nm as compared to $r(Ca^{2+}) = 0.112$ nm (8-coordinated) and $r(Co^{3+}) = 0.0545$ nm and $r(Co^{4+}) = 0.053$ nm as compared to $r(Mn^{3+}) = 0.058$ nm and $r(Mn^{4+}) = 0.053$ nm (6-coordinated) according to Shannon[10]. More specifically, the isotopes ^{84}Sr and ^{59}Co were used for the SIMS analysis. Dense polycrystalline samples of CMO were prepared, the surfaces were polished, and solutions of nitrates of the chemical tracers were drop cast as thin films on the surfaces. After various annealing runs, the diffusion profiles were obtained by depth-profiling using SIMS. EPMA of a cross-section was utilized to determine the tracer distribution and compositional analysis of CMO. The diffusion coefficients are compared to values for A- and B-site diffusion in related perovskites.

Experimental procedure

Powder with nominal composition $Ca_{0.934}MnO_{3-\delta}$ was synthesized by spray pyrolysis (CerPoTech, Norway). The submicron powder was pressed into pellets using a cold isostatic press (CIP) at 200 MPa, followed by sintering in air at 1350 °C for 20 h forming the CMO composite material comprised of 90 vol% $CaMnO_3$ and 10 vol% $CaMn_2O_4$. The sintered pellets were mounted in acetone-dissolvable epoxy resin (Demotec 33, Germany) and polished to 0.25 μm using a diamond abrasive (DP-spray P, Struers, Denmark). Field emission scanning electron microscopy (SEM) (Quanta FEG 200, FEI) was used for the microstructural characterization.

Aqueous solutions of $Sr(NO_3)_2$ and $Co(NO_3)_2$ (0.5 M) were prepared, and drop-cast on the polished surface of polycrystalline CMO samples, followed by drying at 120 °C, yielding nitrate films of 2 – 10 μm. Then the samples were subjected to their respective annealing temperature in the range of 800 to 1200 °C within an annealing time of 96 h, followed by removal of residual tracer by gently polishing to obtain a relatively smooth and uniform film surface for SIMS analysis. The diffusion profiles were acquired by a CAMECA IMS 7f micro analyzer (SIMS, CAMECA, France). A 10 keV beam of oxygen ions (O^{2+}) was used as a primary raster beam over a selected surface area with a raster size of about 150 μm. Additionally, one annealed sample was selected, cut in the direction perpendicular to the film/polycrystalline interface, and polished to 0.25 μm. The polished sample was carbon coated (Emitech K950X) and subjected to elemental X-ray mappings and beam line-scanning using an electron probe micro analyzer (EPMA) (Cameca SX100) under an acceleration voltage of 15 kV with a focused electron beam current of 20 nA. Back-scattered electron (BSE) images of the analyzed areas were taken in the same instrument.

Results and discussions

Figure 1 shows an SEM image of a representative as-sintered polycrystalline CMO sample before diffusion annealing, with an average grain size of about 6 μm and relative density estimated to be approximately 97 % based on weight, geometry, and estimated theoretical density of the CMO composite from pycnometry as well as from SEM images.
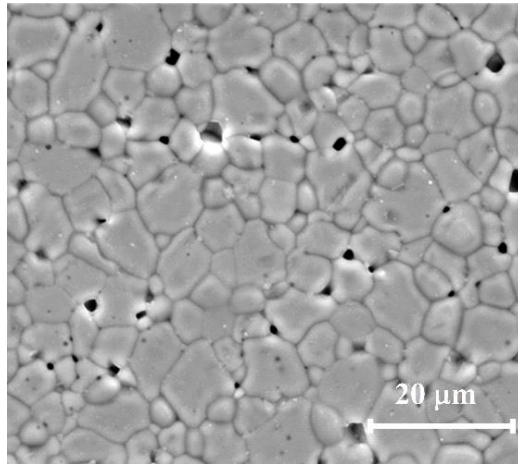
Figure 1. SEM secondary electron (SE) micrograph of the representative microstructure of a polycrystalline sample of CMO.

Figure 2 shows representative SIMS raw data depth profiles of [84]Sr and [59]Co chemical tracers after annealing at 900 and 1000 °C for 96 h, together with their corresponding host cations, i.e., [43]Ca and [55]Mn. The outer few micrometers show seemingly unsystematic features attributed to the deposited layers of tracer compounds. The chemical tracer diffusion profiles inside of this layer are normalized by the host cation profiles for extraction of diffusion coefficients, but we will first discuss some features of the accompanying EPMA mappings (*Figures 3* and *4*).
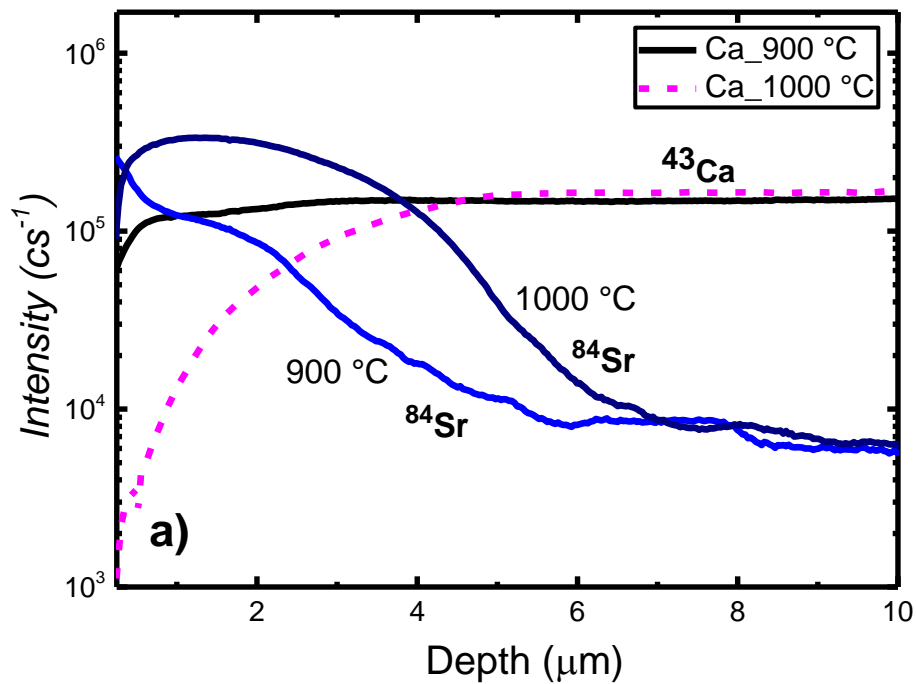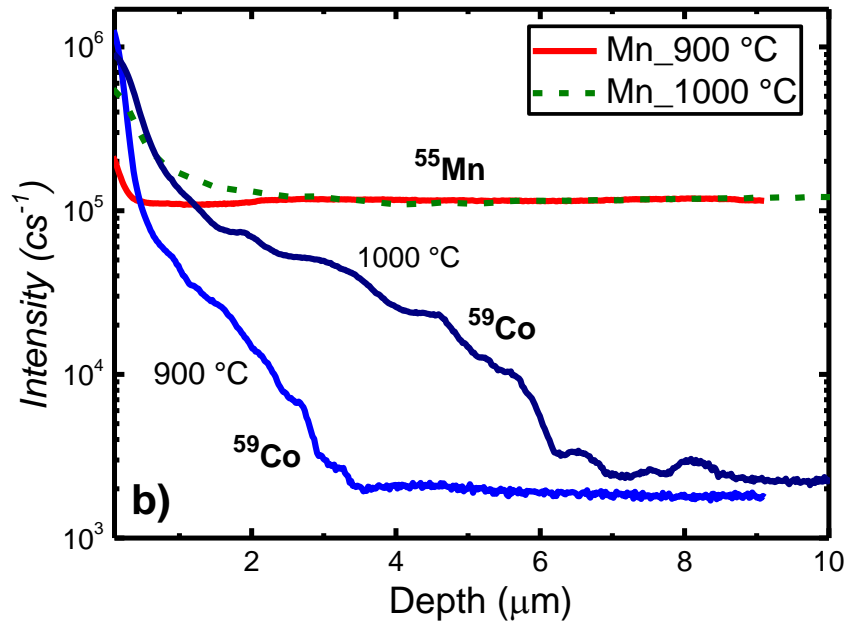
Figure 2. SIMS diffusion profiles showing raw intensity data of ^{84}Sr (a) and ^{59}Co (b) annealed at 900 and 1000 °C for 96 h.

The EPMA Sr mapping in *Figure 3* (c) shows a high concentration of the tracer at the deposited layer and a steep and essentially uniform diffusion front into the bulk sample. The uniform distribution of the Sr tracer in the microstructure, as in *Figure 3* (c), suggests that the Sr tracer diffuses mainly through the bulk, without grain-boundary enhancement.
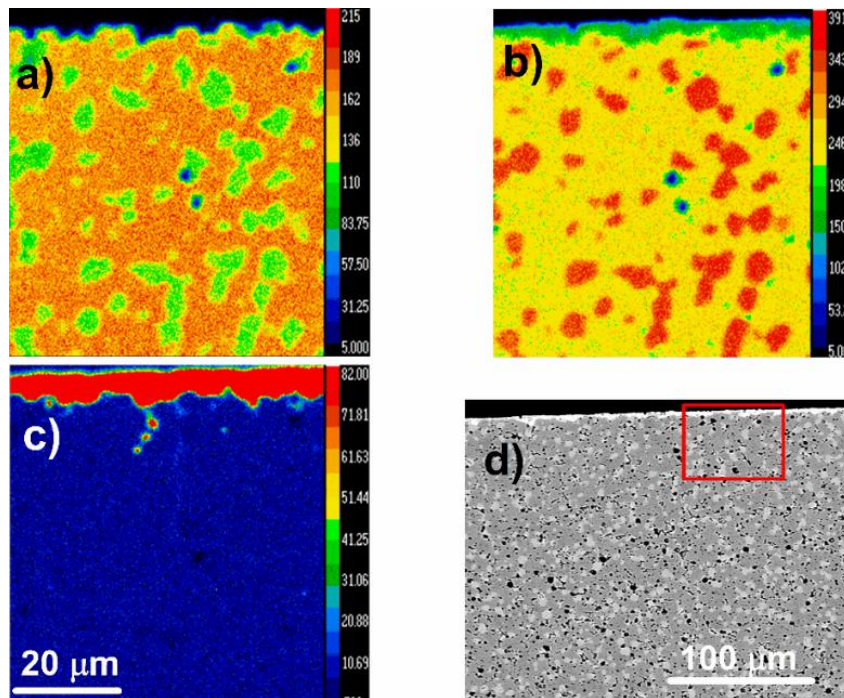

Figure 3. EPMA elemental mappings of Ca (a), Mn (b), Sr (c), and corresponding BSE image (d) of a cross-section at the surface of a polycrystalline sample annealed at 1000 °C for 96 h. The square on the BSE image indicates an area over which X-ray mappings were carried out.

Contrary to the Sr tracer profile mapping, the Co tracer showed longer diffusion paths and a more non-uniform diffusion front with an enhanced concentration of the chemical tracer along the grain boundaries, as seen in *Figure 4* (c).
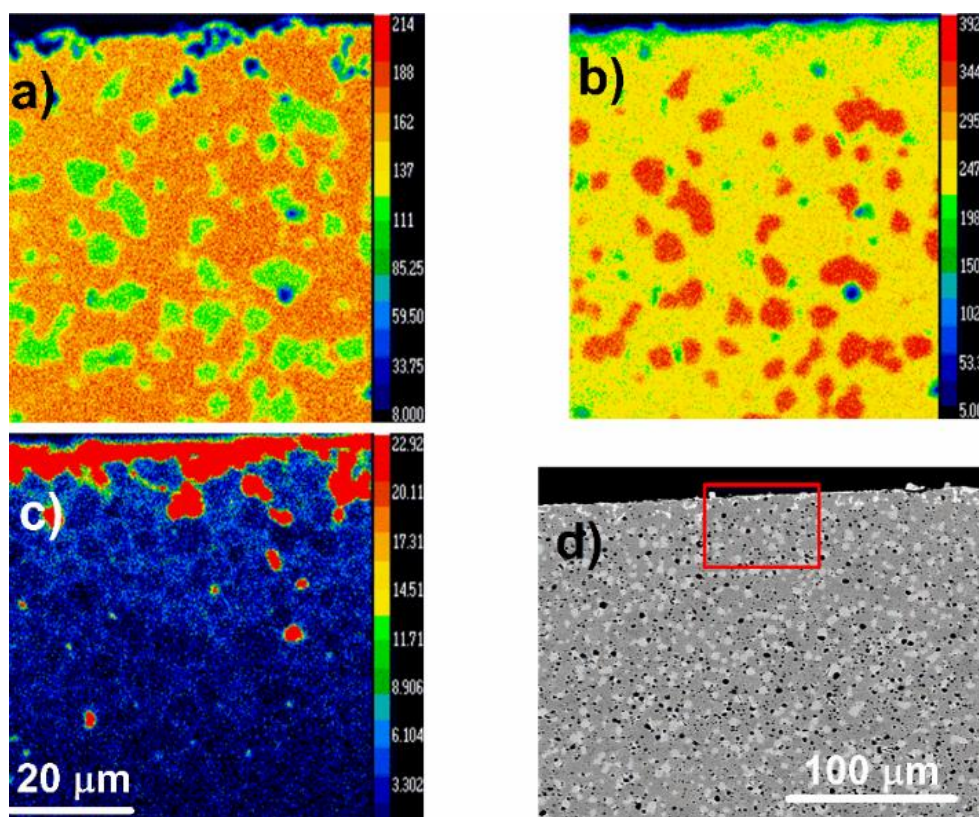

Figure 4. EPMA elemental mappings of Ca (a), Mn (b), Co (c), and corresponding BSE image (d) of the cross-section at the surface of a polycrystalline sample annealed at 1000 °C for 96 h.

The BSE images of *Figures 3* d) and *4* d) show porosities considerably higher than observed and measured for the samples before diffusion annealing. Measurements of the density by weight and geometry confirmed relative densities somewhat above 90%. The reason for this pore growth during diffusion annealing is not clear at present.

The presence of two different phases is apparent from the phase contrast of the BSE images; see *Figures 3* d) and *4* d). The marokite phase ($CaMn_2O_4$) has a higher content of the heavier Mn and hence a higher average atomic mass compared to the perovskite phase ($CaMnO_{3-\delta}$), and hence appears as the brighter phase. The mapping of host cations Ca and Mn in *Figures 3* a) and b) as well as *Figures 4* a) and b) further follows the distribution of perovskite and marokite phases. Based on the phase diagram of CaO-MnO$_x$[11], these two phases are stable and coexist in the temperature range of 890 – 1450 °C, covering both the sintering temperature (1350 °C) and diffusion annealing temperatures (800 – 1200 °C).

To further investigate the effect of the secondary phase (CaMn$_2$O$_4$) on the elemental distribution of the tracers and hence on their diffusion processes, EPMA line-scan measurements were carried out across interfaces between the perovskite and marokite phases in samples annealed at 1000 °C. The quantification of tracers and host cations was made from the line-scan measurements; taken at a distance of approximately 5 – 6 µm away from the deposited tracer film, *Figure 5* (a). The Sr tracer concentration was lower than the detection limit of the instrument (~300 ppm), and therefore it was difficult to deduce the variation in Sr tracer concentration between the two phases. However, we expect that the large Sr^{2+} diffuses slowly on the Ca^{2+} site of the spinel. The concentration of Co tracer was lower in the marokite phase than in the perovskite phase suggesting a lower solubility and/or diffusivity of Co in the marokite phase, *Figure 5* (c). Overall, we may assume that the diffusion of the composite is dominated by the perovskite and that the marokite phase, along with the porosity, only has the minor effect of reducing the diffusion cross-section.
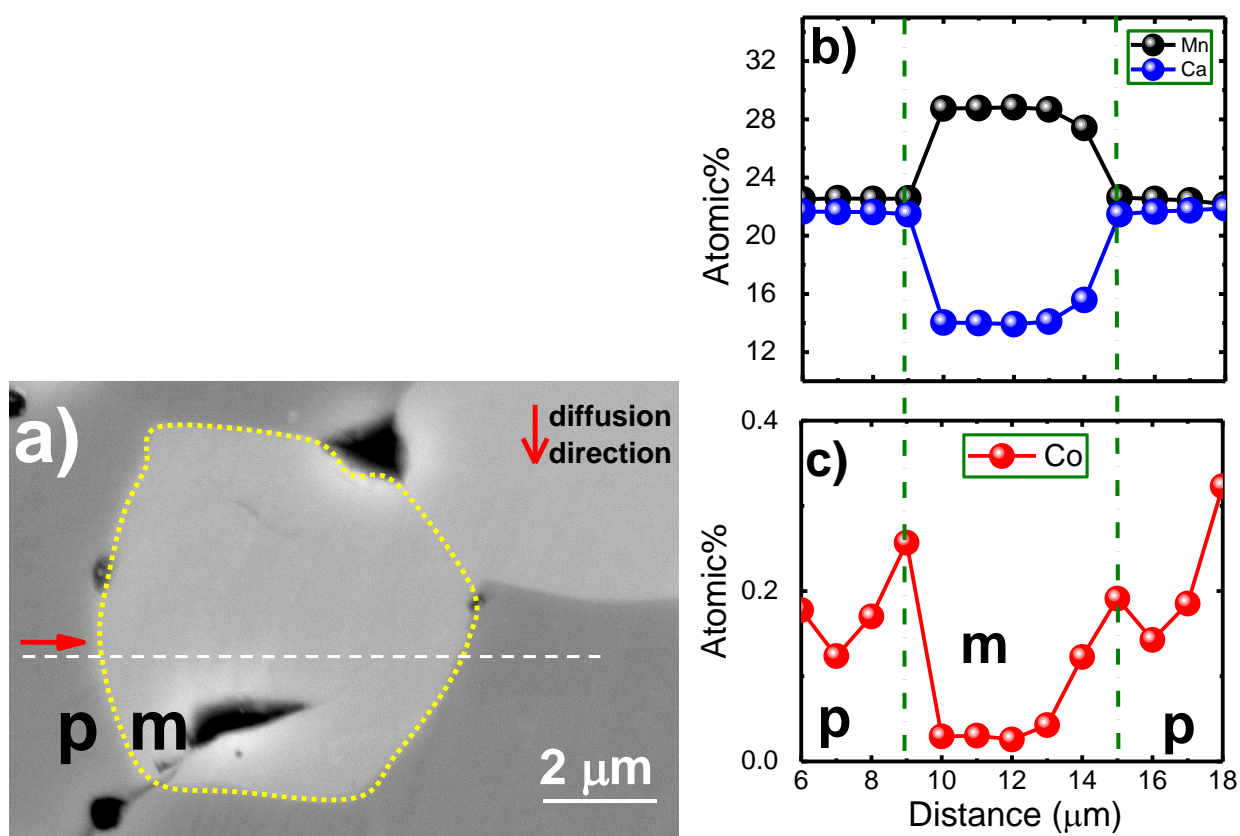

Figure 5. BSE micrograph (a), EPMA elemental analysis of Ca and Mn (b), and Co (c) across the interfaces along the dashed line in (a). The micrograph shows the perovskite (p) and marokite (m) phases with an illustration of the dashed line representing direction of analysis perpendicular to the tracers' diffusion direction.

As expected, the Ca:Mn ratios are approximately 1:1 for the perovskite phase and 1:2 in the spinel. Detailed analysis of the line-scan results suggested that the perovskite matrix had a composition of

$Ca_{1-x}MnO_{3-\delta}$, where x was in the range 0.02 - 0.07 and the oxygen under-stoichiometry (δ) was in the range 0.30 - 0.46. The Ca deficiency may be constituted by Ca-vacancies ($v_{Ca}^{//}$), which, together with the conduction-band defect electrons ($e^{/}$) compensate the oxygen vacancies ($v_O^{\bullet\bullet}$).

Fick's second law of diffusion with a thin-film source model can be used to estimate the lattice bulk diffusion coefficients of each of the chemical tracers according to[12]:

$$C(x,t) = C_o(t)exp\left(-\frac{x^2}{4D_Lt}\right) \tag{1}$$

Here, $C(x,t)$ is the concentration of the diffusing species at a penetration distance x (cm) for an annealing time of t (s). C_o is the surface concentration, and D_L (cm^2/s) is the lattice diffusion coefficients of the diffusing species. The D_L is equivalent to the effective diffusivity, D_{eff} in polycrystalline materials[13] assuming that the diffusion kinetics is type A based on Harrison's classifications of diffusion processes[14]. By normalizing the intensity obtained from SIMS (cf. *Figure 2*), i.e. normalizing Sr intensity against Ca and that of Co against Mn, profiles are obtained which can be fitted to Eq. (1) to calculate the D_L. According to Eq. (1) a plot of the log($C(x,t)$) against penetration depth, x^2 yields a linear region, from which D_L can be calculated from the slope. For instance, *Figure 6* (a) and (b) show plots of the logarithm of normalized concentrations against x^2 for [84]Sr and [59]Co tracers, respectively. Linear regression to region (I) yields the lattice diffusivity of the tracers. Accordingly, Sr had a lattice diffusivity of about 1.0×10^{-14} cm^2/s at 1000 °C whereas that of Co was about 1.5×10^{-12} cm^2/s at 1200 °C.
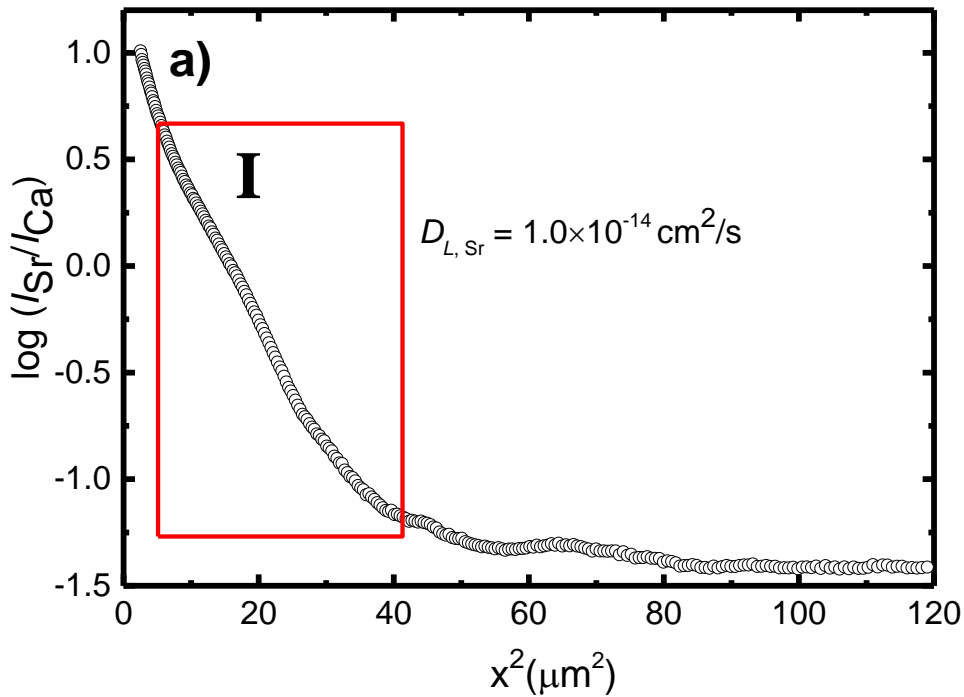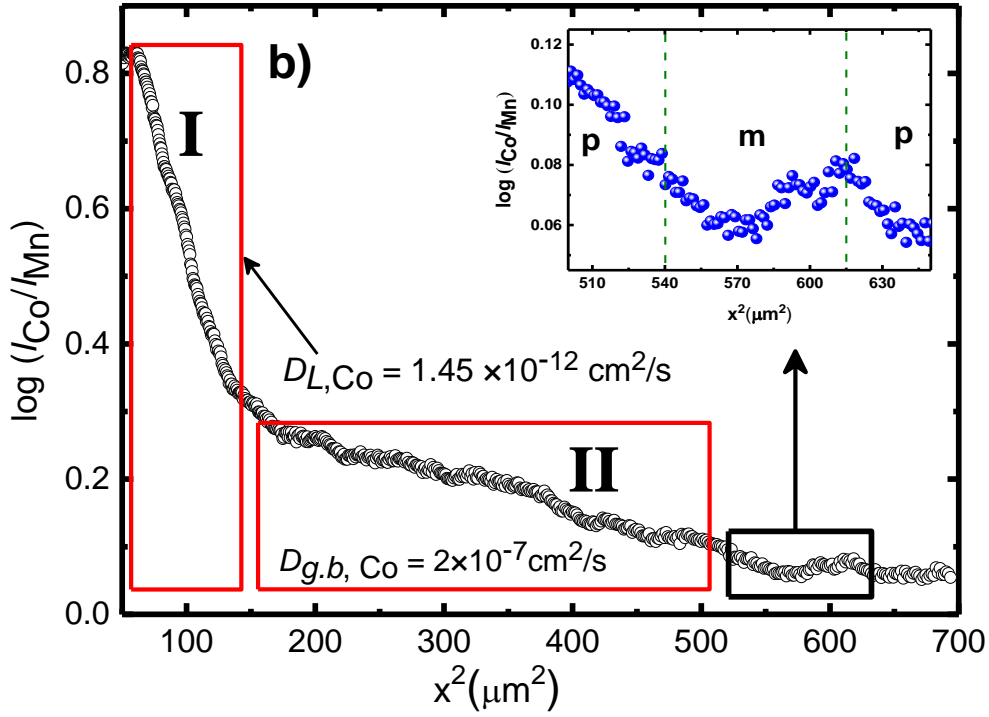
Figure 6. Diffusion depth profiles for Sr (a) at 1000 °C and Co (b) at 1200 °C. The annealing time was 96 h. The lattice diffusion coefficients were extracted from region (I) in (a) and (b), whereas grain-boundary diffusion coefficients were obtained from region (II) in plot (b). The inset in (b) shows the Co intensity that changed across the perovskite (p)/marokite (m) phase interfaces upon ion sputtering showing a formation of plateau regions because of the presence of the secondary phase.

The higher content of Mn in the marokite phase compared to the perovskite phase region (cf. *Figure 5* (b)) resulted in the formation of shallow plateau regions in the profile (cf. *Figure 2* (b) and inset of *Figure 6* (b)). The opposite effect would be observed for Sr chemical tracer profile, *Figure 2* (a).

The grain-boundary diffusion coefficient of the ^{59}Co tracer can be obtained from the diffusion profile in the deepest penetration region, the grain-boundary tail, using an approximated solution equation given by Whipple-Le Claire as[15-17]

$$swD_{\text{g.b}} = 0.3292 \left(\frac{D_L}{t}\right)^{1/2} \left(-\frac{\delta logC}{\delta x^{6/5}}\right)^{-5/3} \qquad (2)$$

where s is the segregation factor, w is the grain boundary width (cm), $D_{g.b}$ is the grain-boundary diffusion coefficient (cm^2/s), and the other parameters have their usual meanings. A plot of log ($C_{x,t}$) against the penetration depth, $x^{6/5}$ showed good linearity in the grain-boundary tail (region II of *Figure 6* (b)), from which a slope equivalent to the term $\left(-\frac{\delta logC}{\delta x^{6/5}}\right)$ in equation (2) can be obtained. This enables to calculate the triple product, $swD_{g.b}$. Assuming a unit segregation factor and about 1.0 nm grain boundary thickness, which seems typical for most perovskite materials, an estimate of the

grain-boundary diffusion coefficient can be obtained from equation (2). The corresponding grain-boundary diffusion coefficient of the tracer at the specified conditions was about 2×10^{-7} cm^2/s at 1200 °C.

The calculated diffusion coefficients are plotted versus inverse temperature in *Figure 7*. The pre-exponential and activation energies of the diffusion coefficients are obtained by fits to equation (3).

$$D_i = D_o exp\left(\frac{-E_a}{RT}\right) \tag{3}$$

Here, D_i is the diffusion coefficient of individual cations, D_o is the pre-exponential, E_a is the activation energy (which may comprise formation and diffusion of point defects), R is the universal gas constant, and T is absolute temperature.
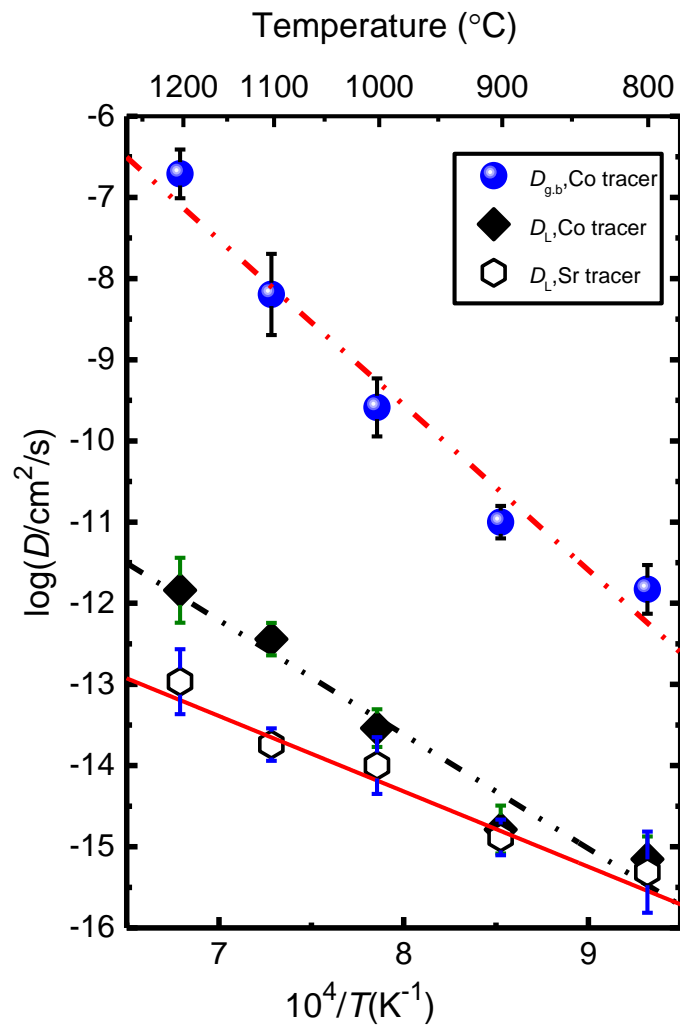

Figure 7. Arrhenius plot showing the lattice diffusion coefficients of Sr and Co and the grain-boundary diffusion coefficients of Co in polycrystalline CMO.

Each value in the plot contains the confidence interval from the linear regression of fitting the diffusion profile to equation (1). The diffusion coefficients according to equation (3) are also represented as follows:

$$D_{\text{L,Co}} = 10^{-2.4\pm1.3} exp\left(\frac{-270\pm30 \text{ (kJ/mol)}}{RT}\right) (\text{cm}^2/\text{s}) \tag{4}$$

$$D_{\text{g.b,Co}} = 10^{6.7\pm1.7} exp\left(\frac{-380\pm40 \text{ (kJ/mol)}}{RT}\right) (\text{cm}^2/\text{s}) \tag{5}$$

$$D_{\text{L,Sr}} = 10^{-6.0\pm1.1} exp\left(\frac{-210\pm30 \text{ (kJ/mol)}}{RT}\right) (\text{cm}^2/\text{s}) \tag{6}$$

The confidence intervals are rounded-off values from the linear regression of the Arrhenius plots. A-site diffusion exhibits a lower activation enthalpy than B-site diffusion, but the difference is hardly beyond the uncertainty and may be correlated with the difference in the pre-exponential. The similarity in the magnitude of the diffusion coefficients may, in any case, indicate that A and B site diffusion take place via the same mechanism and may use the same (or both) sites, as suggested for other perovskites, for example, bulk diffusion of Mg and Si in $MgSiO_3$[18]. However, for most perovskites A-site diffusion is slower compared to B-site diffusion, and the reason for the similarities between A- and B-site in our material may be the A-site vacancies which will enhance diffusion on this site. The relatively small activation enthalpy for the A-site diffusion process may also be explained by the presence of A-site vacancies so that only the migration enthalpy of these remains.

The activation energies calculated for lattice and grain-boundary diffusion of Co on B-site were 270±30 and 380±40 kJ/mol, respectively, which may comprise defect formation (ΔH_d^o) and defect mobility (ΔH_m) enthalpies. The significantly higher activation energy and many orders of higher pre-exponential of the enhanced grain boundary diffusion are noteworthy, but have been reported for several polycrystalline materials[11, 19], in particular those with mixed valency cations. Waller et al.[20, 21] reported a high activation energy of Mn grain-boundary diffusion in polycrystalline YSZ and assigned it to mixed manganese oxidation states, and Čebašek et al.[22] reported the same for Co diffusion in $La_2NiO_{4+\delta}$.

The samples held some porosity, and the pores grew somewhat during the annealing, for unknown reasons. The possible effects of the pores and their growth should partly be to reduce diffusion cross-section while offering gas phase short-circuit diffusion and enhanced diffusion on internal surfaces, especially of Co, similar to enhanced grain boundary diffusion. As, however, the total pore volume is modest and seemingly non-percolating, we believe that its effects can to a first approximation be disregarded.

A comparison of the present diffusivity data to literature values of A- and B-site diffusion coefficients to similar oxide materials is presented in *Figure 8* and *Figure 9*, respectively. The Sr diffusion in polycrystalline CMO exhibited higher diffusivities than in most $A^{II}B^{IV}O_3$ perovskites, for example, Sr diffusion in $BaTiO_3$. The Sr diffusivity in single crystal $(La,Sr)TiO_3$ also showed lower diffusivity than that of the Sr diffusion of this work. This may be attributed to the existence of Ca-vacancies on A-site in the perovskite phase of the composite material. On the other hand, the A-site diffusivities of the present work were lower than those in $A^{III}B^{III}O_3$ perovskites, for instance, Nd in polycrystalline $NdFeO_3$ and Y in polycrystalline $YCrO_3$ at comparable temperatures.
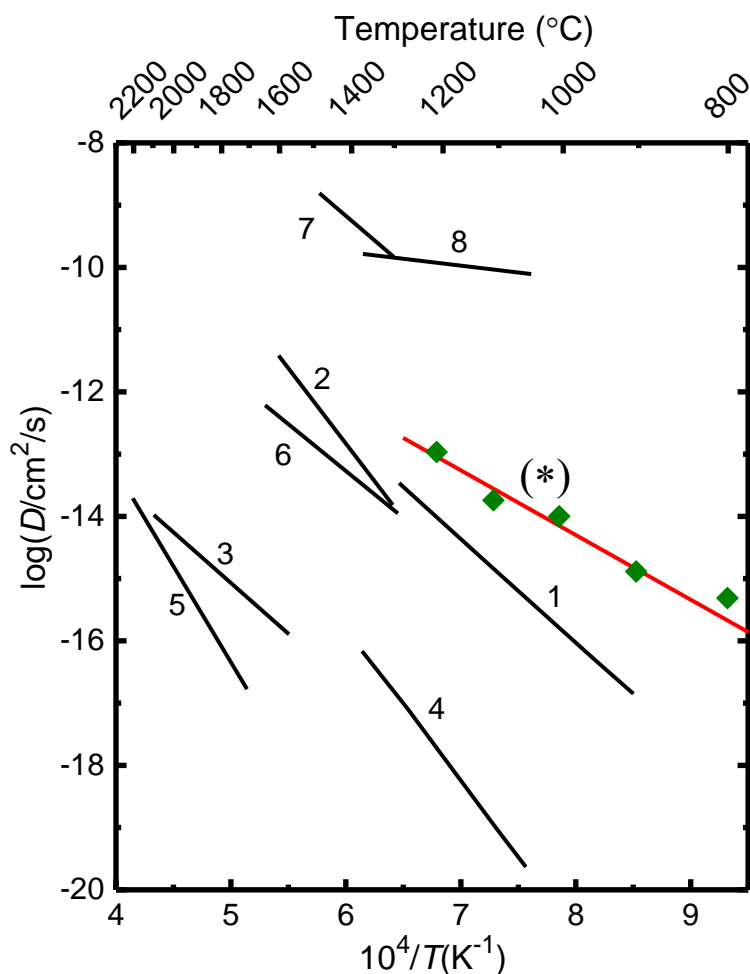

Figure 8. A comparison of A-site diffusion coefficient of CMO with selected perovskites in an Arrhenius type plot. (*) ^{84}Sr diffusion in CMO (lattice, this work),(1) Ba in BaTiO$_3$ [23], (2) La in LaCrO$_3$ [24], (3) Mg in MgSiO$_3$ [18], (4) Sr in BaTiO$_3$ (single crystal) [25], (5) ^{88}Sr in (Sr,La)TiO$_3$ (single crystal) [26], (6) ^{90}Sr in SrTiO$_3$ [27], (7) Y in YCrO$_3$ [28], (8) Nd in NdFeO$_3$ [29].

B-site (Mn-site) diffusion coefficients—both lattice and grain-boundary diffusivities—are compared to the literature results of various perovskite materials in *Figure 9*. In all cases, faster diffusion of Co was observed in the polycrystalline composite of CMO compared to $A^{II}B^{IV}O_3$ perovskites such as diffusion of Ni in $BaTiO_3$ and diffusion of Si in $MgSiO_3$. On the other hand, compared to diffusion

on the B-site in $A^{III}B^{III}O_3$ perovskites such as Mn in LaCoO$_3$[30], Mn in LaMnO$_3$[31], and Co in LaCoO$_3$[32], the Co chemical tracer diffusion in CMO exhibited slower diffusion yet with similar activation energies. In the composite sample, manganese exists in its mixed oxidation states ranging from Mn^{3+} of the marokite phase to different ratios of Mn^{3+} and Mn^{4+} in the perovskite phase. The ratios are mainly defined by the amount of oxygen under-stoichiometry (δ) in the latter phase[11]. This may explain why the diffusion on the Mn-site in the current polycrystalline material is faster than that of the literature values of most corresponding $A^{II}B^{IV}O_3$ perovskites, as seen in *Figure 9*. Lastly, it should be repeated that the diffusion coefficients reported in this work for CaMnO$_3$ are probably conservative, since the marokite spinel phase and the pores will have reduced the diffusion cross-section somewhat.
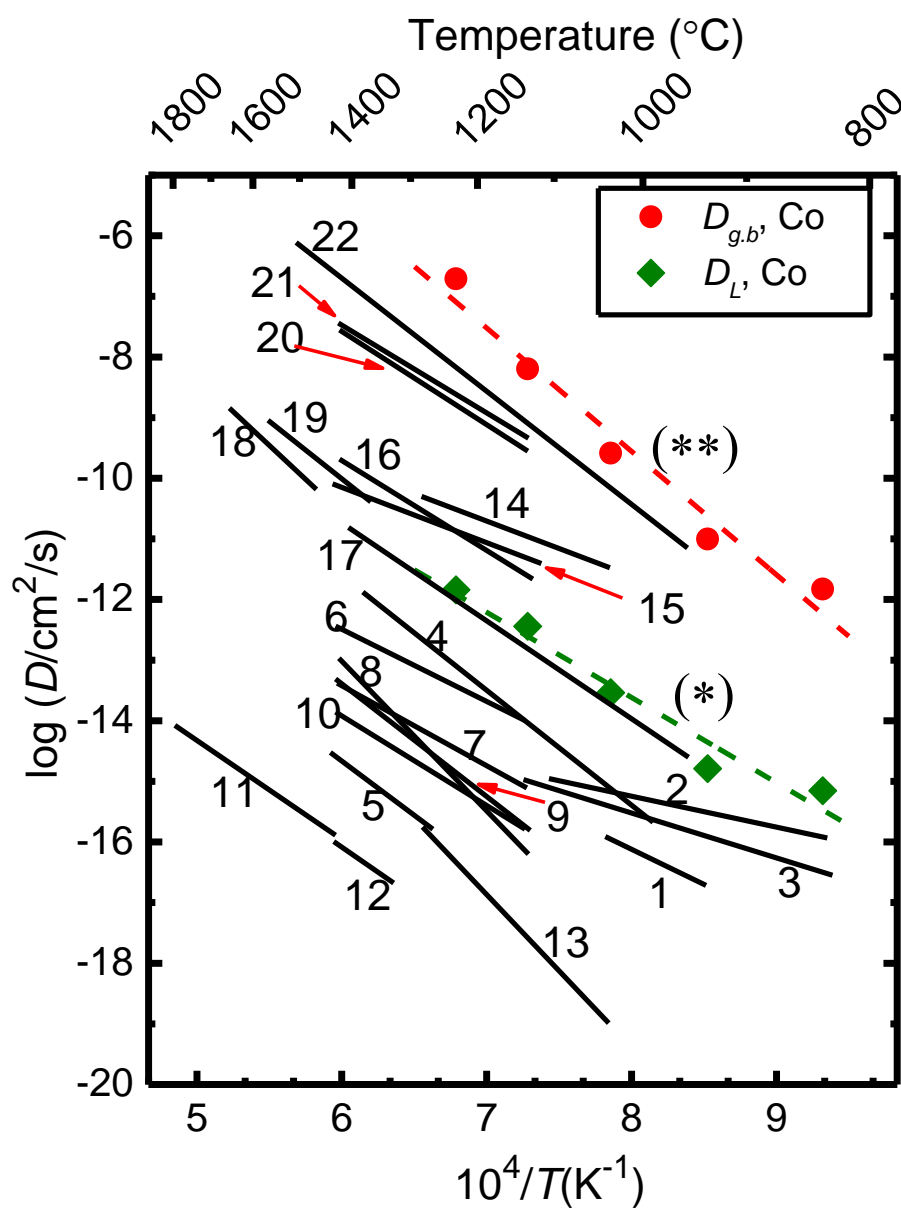
Figure 9. A comparison of the B-site diffusion coefficient of CMO with selected perovskites in an Arrhenius type plot. (*) Co in CMO (lattice, this work), 1) ^{50}Cr in (La, Ca)CrO$_3$ [33], 2) Fe in (La, Sr)CoO$_3$ [34], 3) Fe in (La, Sr)FeO$_3$ [34], 4) Fe in LaFeO$_3$ [35], 5) Fe in NdFeO$_3$ [29], 6) Ni in Ba(Ho,Ti)O$_3$ [36], 7) Ni in BaTiO$_3$ [36], 8) Ni in BaTiO$_3$ (single crystal) [36], 9) ^{141}Pr in LaCoO$_3$ [37], 10) ^{141}Pr in LaFeO$_3$ [37], 11) Si in MgSiO$_3$ [18], 12) ^{49}Ti in (La,Sr)TiO$_3$ (single crystal) [38], 13) Zr in BaTiO$_3$(single crystal) [39], 14) Co in LaCoO$_3$ (bulk diffusion) [32], 15) Mn in LaCoO$_3$ [30] 16) Mn in LaMnO$_3$ [31] 17) Yb in YSZ(grain boundary) [40], 18) Zr in BaZrO$_3$ (grain boundary) [41], 19) Pr in LaFeO$_3$(grain boundary) [37], 20) Pr in LaCoO$_3$(grain boundary) [37], 21) Co in La$_2$NiO$_4$ (grain boundary) [22], (**) Co in CMO (grain boundary, this work).

Conclusions

In summary, Sr and Co chemical tracer diffusivities on the A- and B-site, respectively, of perovskite CaMnO$_{3-\delta}$ in a CaMnO$_{3-\delta}$/CaMn$_2$O$_4$ composite were determined in the temperature range 800 – 1200 °C. The A- and B-site lattice diffusivities were of similar magnitude. The activation enthalpy and pre-exponential were both lower for the A-site than for the B-site, but this may be a correlation within uncertainties. It can be argued based on EPMA analysis that the perovskite has Ca-vacancies which enhance A-site diffusivity compared to most A^{II}B^{IV}O$_3$ perovskites. B-site diffusion of Co showed an additional enhanced grain boundary tail with a large activation energy of about 380±40 kJ/mol compared to lattice diffusion with 270±30 kJ/mol. The existence of A-site vacancies may also have contributed to the observed faster diffusion of the Co chemical tracer. Diffusivities on the B-site—both bulk and grain boundary—showed higher values than similar perovskite-structured materials, often attributed to mixed B-site cation oxidation states. The formation of a secondary phase (Ca$_3$Co$_{2-y}$Mn$_y$O$_6$) when a *p-n* junction is established directly between Ca$_3$Co$_{3.92}$O$_{9-\delta}$ (CCO) and CaMnO$_{3-\delta}$ (CMO) may thus in part be attributed to the fast diffusion process on the B-site in the polycrystalline CMO. Computational determination of enthalpies of formation and mobility for cations, ΔH_d^o and ΔH_m, respectively, would be interesting to correlate the present experimental activation energies to that of theoretical.

Conflict of Interests

There are no conflicts of interest to declare.

Acknowledgements

References

1.   T. J. Seebeck, *Annalen der Physik*, 1826, **82**, 253-286.

2.   J. P. Heremans, *Nature*, 2014, **508**, 327-328.

3.   M. Wagner, G. Span, S. Holzer and T. Grasser, *Semicond. Sci. Technol.*, 2007, **22**, S173.

4.   M. Schrade, H. Fjeld, T. G. Finstad and T. Norby, *J. Phys. Chem. C*, 2014, **118**, 2908-2918.

5.   M. Schrade, S. Casolo, P. J. Graham, C. Ulrich, S. Li, O.-M. Løvvik, T. G. Finstad and T. Norby, *J. Phys. Chem. C*, 2014, **118**, 18899-18907.

6.   M. Schrade, R. Kabir, S. Li, T. Norby and T. G. Finstad, *J. Appl. Phys.*, 2014, **115**, 103705.

7.   N. Kanas, *Unpublished work*, 2018.

8.   X. Han, Y. Hu, J. Yang, F. Cheng and J. Chen, *Chem. Commun.*, 2014, **50**, 1497-1499.

9.   J. Du, T. Zhang, F. Cheng, W. Chu, Z. Wu and J. Chen, *Inorg. Chem.*, 2014, **53**, 9106-9114.

10.   R. D. Shannon, *Acta Crystallogr., Sect. A*, 1976, **32**, 751-767.

11.   H. S. Horowitz and J. M. Longo, *Mater. Res. Bull.*, 1978, **13**, 1359-1369.

12.   J. Crank, *The mathematics of diffusion*, Oxford university press, 1979.

13.   E. W. Hart, *Acta Metallurgica*, 1957, **5**, 597.

14.   L. G. Harrison, *Trans. Faraday Soc.*, 1961, **57**, 1191-1199.

15.   R. T. P. Whipple, *The London, Edinburgh, and Dublin Philosophical Magazine and Journal of Science*, 1954, **45**, 1225-1236.

16.   A. D. L. Claire, *Br. J. Appl. Phys.*, 1963, **14**, 351.

17.   I. Kaur, W. Gust and Y. Mishin, *Fundamentals of grain and interphase boundary diffusion*, J. Wiley, Chichester, 1995.

18.   J. Xu, D. Yamazaki, T. Katsura, X. Wu, P. Remmert, H. Yurimoto and S. Chakraborty, *J. Geophys. Res.: Solid Earth*, 2011, **116**.

19.   E. I. Leonidova, I. A. Leonidov, M. V. Patrakeev and V. L. Kozhevnikov, *J. Solid State Electrochem.*, 2011, **15**, 1071-1075.

20.   D. Waller, J. D. Sirman and J. A. Kilner, *Manganese diffusion in single crystal and polycrystalline yttria stabilised zirconia*, 1997.

21.   M. Kilo, M. A. Taylor, C. Argirusis, G. Borchardt, B. Lesage, S. Weber, S. Scherrer, H. Scherrer, M. Schroeder and M. Martin, *J. Appl. Phys.*, 2003, **94**, 7547-7552.

22.   N. Čebašek, R. Haugsrud, Z. Li and T. Norby, *J. Am. Ceram. Soc.*, 2013, **96**, 598-605.

23.   A. GARCIAVERDUCH and R. Lindner, *ARKIV FOR KEMI*, 1953, **5**, 313-316.

24.   T. Akashi, M. Nanko, T. Maruyama, Y. Shiraishi and J. Tanabe, *J. Electrochem. Soc.*, 1998, **145**, 2090-2094.

25.   S. Koerfer, R. A. De Souza, H.-I. Yoo and M. Martin, *Solid State Sci.*, 2008, **10**, 725-734.

26. K. Gömann, G. Borchardt, M. Schulz, A. Gömann, W. Maus-Friedrichs, B. Lesage, O. Kaïtasov, S. Hoffmann-Eifert and T. Schneller, *Phys. Chem. Chem. Phys.*, 2005, **7**, 2053-2060.

27. W. Rhodes and W. Kingery, *J. Am. Ceram. Soc.*, 1966, **49**, 521-526.

28. K. i. Kawamura, A. Saiki, T. Maruyama and K. Nagata, *J. Electrochem. Soc.*, 1995, **142**, 3073-3077.

29. B. O. F. M.M. Pavlyuchenko, I. E. Shimanovich, S.A., 1970.

30. M. Palcut, R. Knibbe, K. Wiik and T. Grande, *Solid State Ionics*, 2011, **202**, 6-13.

31. S. Miyoshi and M. Martin, *Phys. Chem. Chem. Phys.*, 2009, **11**, 3063-3070.

32. M. Palcut, K. Wiik and T. Grande, *J. Phys. Chem. B*, 2007, **111**, 2299-2308.

33. N. Sakai, K. Yamaji, T. Horita, H. Negishi and H. Yokokawa, *Solid State Ionics*, 2000, **135**, 469-474.

34. H. Kishimoto, N. Sakai, T. Horita, K. Yamaji, M. E. Brito and H. Yokokawa, *Solid State Ionics*, 2007, **178**, 1317-1325.

35. J. B. Smith and T. Norby, *Solid State Ionics*, 2006, **177**, 639-646.

36. J.-i. Itoh, I. Yashima, N. Ohashi, I. Sakaguchi, H. Haneda and J. Tanaka, *J. Ceram. Soc. Jpn.*, 2001, **109**, 955-959.

37. M. Palcut, J. S. Christensen, K. Wiik and T. Grande, *Phys. Chem. Chem. Phys.*, 2008, **10**, 6544-6552.

38. K. Gomann, G. Borchardt, A. Gunhold, W. Maus-Friedrichs and H. Baumann, *Phys. Chem. Chem. Phys.*, 2004, **6**, 3639-3644.

39. S. Koerfer, R. A. De Souza, H.-I. Yoo and M. Martin, *Solid State Sci.*, 2008, **10**, 725-734.

40. S. Swaroop, M. Kilo, C. Argirusis, G. Borchardt and A. H. Chokshi, *Acta Mater.*, 2005, **53**, 4975-4985.

41. R. Sazinas, I. Sakaguchi, I. Hasle, J. M. Polfus, R. Haugsrud, M.-A. Einarsrud and T. Grande, *Phys. Chem. Chem. Phys.*, 2017, DOI: 10.1039/C7CP04039C.